Enzyme Scaffolds with Hierarchically Defined Properties via 3D Jet Writing

Anke Steier, Barbara Schmieg, Yannic Irtel von Brenndorff, Manuel Meier, Hermann Nirschl, Matthias Franzreb, and Joerg Lahann*

The immobilization of enzymes into polymer hydrogels is a versatile approach to improve their stability and utility in biotechnological and biomedical applications. However, these systems typically show limited enzyme activity, due to unfavorable pore dimensions and low enzyme accessibility. Here, 3D jet writing of water-based bioinks, which contain preloaded enzymes, is used to prepare hydrogel scaffolds with well-defined, tessellated micropores. After 3D jet writing, the scaffolds are chemically modified via photopolymerization to ensure mechanical stability. Enzyme loading and activity in the hydrogel scaffolds is fully retained over 3 d. Important structural parameters of the scaffolds such as pore size, pore geometry, and wall diameter are controlled with micrometer resolution to avoid mass-transport limitations. It is demonstrated that scaffold pore sizes between 120 μm and 1 mm can be created by 3D jet writing approaching the length scales of free diffusion in the hydrogels substrates and resulting in high levels of enzyme activity (21.2% activity relative to free enzyme). With further work, a broad range of applications for enzyme-laden hydrogel scaffolds including diagnostics and enzymatic cascade reactions is anticipated.

1. Introduction

The use of enzymes as catalysts is an important approach in the move toward greener methodologies to replace environmentally harmful organic synthesis. Enzymes are conventionally used in homogenous systems due to high conversion rates as well as regio- and stereoselectivity, thereby eliminating the formation of by-products.[1] However, commercial utilization of enzymes is hampered by the lack of stability and limited recycling capacity.[2] As a solution to the limitations of homogeneous systems, enzyme immobilization onto substrates through physical or covalent bonding has been widely adopted, particularly for less abundant enzymes.[3] In addition, enzyme immobilization enables the use in continuous flow reactors, which can lead to increased throughput.[4,5] The physical and chemical properties of the support material as well as the nature of the enzyme are decisive factors in enzyme immobilization.[6] Enzyme immobilization methods can be classified into three different categories: i) intermolecular cross-linking between the enzyme and a filler molecule, ii) conjugation of the enzyme to a support, and iii) physical entrapment of the enzyme inside of a matrix.[7] Compared to covalent binding (i+ii), which requires optimization of tailored chemical reactions,[8] physical entrapment is applicable to different enzymes without the need of expensive case-to-case alterations. The simple and fast process of physical entrapment in a porous matrix allows for enzyme immobilization over a wide pH range as well as to nonpurified material like untreated cell extract.[9,10] Moreover, reduced enzyme activity due to steric hindrance can be avoided, and no additional crosslinking reagents are necessary.[11]

Even though there are many advantages to physically entrapping enzymes within a matrix, there are also important shortcomings that are yet to be addressed, including uneven distribution of enzymes inside the matrix material, slow diffusion of the substrate to the active site, and microenvironmental effects like ionic strength or inhibition effects.[12] One of the most important parameters that directly affects enzyme activity is the chemical stability of the enzyme inside the matrix material.[13] To address current drawbacks, emerging trends are moving toward highly porous polymer host structures. Ideally, the enzymes are embedded in a matrix comprised of narrow structures that are interfaced by interconnected pores to facilitate diffusion, while ensuring that the enzymes are retained in the support matrix.

One of the most frequently used materials for enzyme immobilization by entrapment are silica sol-gels prepared by

A. Steier, Dr. B. Schmieg, Y. Irtel von Brenndorff, Prof. M. Franzreb, Prof. J. Lahann
Institute of Functional Interfaces (IFG)
Karlsruhe Institute of Technology (KIT)
Hermann-von-Helmholtz-Platz 1, Eggenstein-Leopoldshafen 76344, Germany
E-mail: lahann@umich.edu
M. Meier, Prof. H. Nirschl
Institute of Mechanical Process Engineering and Mechanics (MVM)
Karlsruhe Institute of Technology (KIT)
Straße am Forum 8, Karlsruhe 76131, Germany
Prof. J. Lahann
Biointerfaces Institute and Departments of Chemical Engineering
Materials Science and Engineering, Macromolecular Science and Engineering and Biomedical Engineering
University of Michigan
Ann Arbor, MI 48109, USA

**ADVANCED
SCIENCE NEWS**
www.advancedsciencenews.com
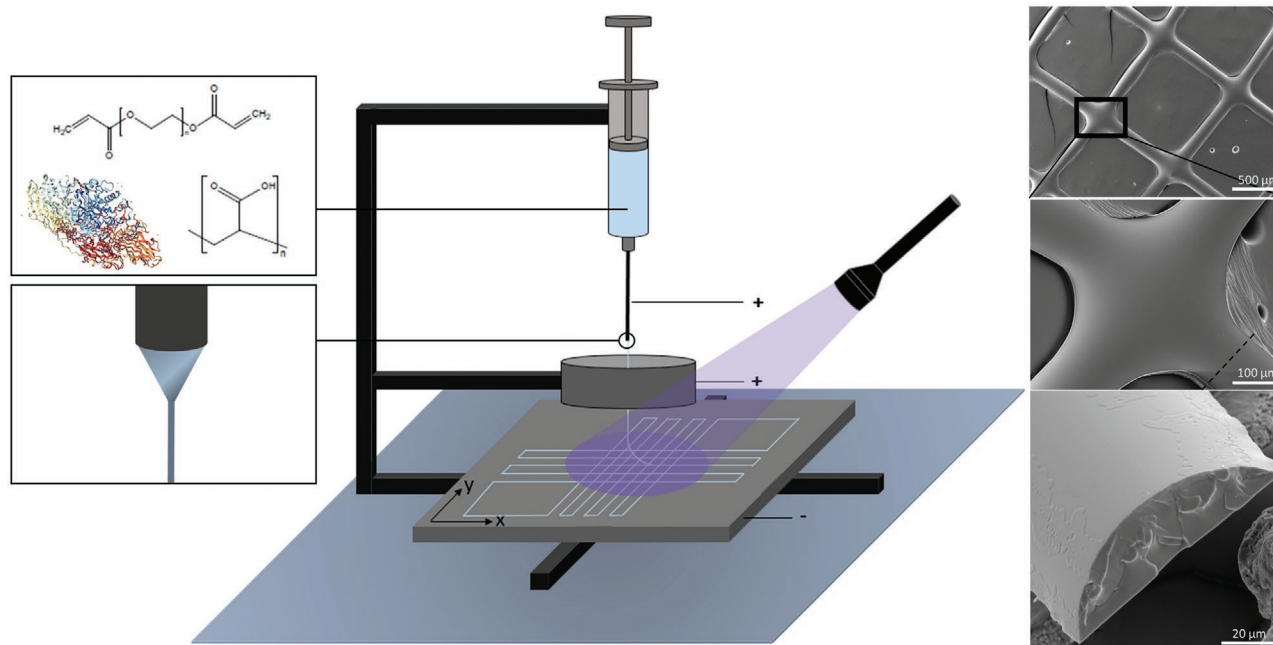
**Macromolecular
Bioscience**
www.mbs-journal.de

Figure 1. 3D jet writing of hydrogel fibers. The process allows to yield precisely oriented hydrogel fibers loaded with biological active material. Elongation of the jetting ink through an applied electric field results in 6.5 times thinner patterned filaments compared to extrusion-based printing.

hydrolytic polymerization of tetraethoxysilane.[7] Sol-gels are benign to enzymes and do not form chemical bonds with the enzyme.[1] The material is porous in nature with a tunable porosity and a negligible swelling behavior, which prevent enzyme leakage. Unfortunately, sol-gels exhibit considerable structural changes during drying, which is associated with shrinkage and a decrease in porosity.[7,14] By an optimized synthesis procedure, silica aerogels can retain 90% of its original porosity.[15] However, the manufacturing process of aerogels is still based on organic solvents and therefore limits the broader application to enzymes.[16]

An emerging approach is to entrap biocatalysts in natural or synthetic hydrogels. Hydrogels are a very promising material class because they provide an aqueous microenvironment for proteins. Hydrogels can support physical entrapment of enzymes, while locally maintaining an aqueous environment suitable for biological processes.[17]

Besides biopolymers like gelatin, alginate, or agarose hydrogels,[4,18] synthetic hydrogels made of polyvinyl alcohol, so-called Lentikats, have been widely used for enzyme immobilization.[19] Unfortunately, most gels do not have the right network structure to prevent enzyme leaching from the swollen hydrogels in an aqueous environment. This limits the use of hydrogel networks to nonaqueous media or large enzymes including crosslinked protein aggregates.[7,20]

Advantages of using synthetic poly(ethylene glycol) (PEG)-based hydrogels include their superior chemical and biological stability and the tunable porosity of the hydrogel network based on the appropriate choice of the chain length of the PEG segment. Their variable processibility makes PEG-based hydrogels a very attractive support material, especially if the hydrogel can be 3D-printed into optimized shapes.[21] Although extrusion-based printing can proceed under mild process conditions, they typically are limited by low resolution caused by the nozzle diameter of the printer and the applied pressure.[4,22]

Electrospinning is a method that allows the production of thin polymer fibers in the micro- and nanometer range with a large spectrum of different polymers and was already used for cell encapsulation.[23,24] Unfortunately, random deposition of the fibers on the collector due to bending and whipping instabilities based on the applied electric field is common.[25] Important exceptions include melt-electrospinning or near-field jetting, but the former requires heat and the latter still uses organic solvents as the evaporation rates must be fast due to the short travel distances of the jet.[26]

Circumventing both issues, 3D jet writing offers the advantage of precise patterning of polymer fibers, while ensuring at the same time a long jet path.[27] By applying an electric field, the fluid ink droplet on the needle gets deformed into a conical droplet, called the Taylor cone. A charged ink jet accelerates toward the grounded collector, is elongated by the electric field, and results in thinner patterned filaments compared to extrusion-based printing. By applying a second ring electrode, the direction of the electric potential is modified toward the center of the circular electrode and suppresses the initiation of the whipping instabilities.[28] Combining this setup with a computer-controlled x–y stage allows for accurate patterning of the jetting ink (**Figure 1**). So far, 3D jet writing has been limited to poly(lactic-co-glycolic acid) (PLGA) polymers in a chloroform-dimethylformamide mixture as solvent, which has restricted its use for enzyme encapsulation.

In this paper, we present a new 3D jet writing approach using water-based inks to entrap enzymes inside hydrogel architectures. The material system is based on PEG and
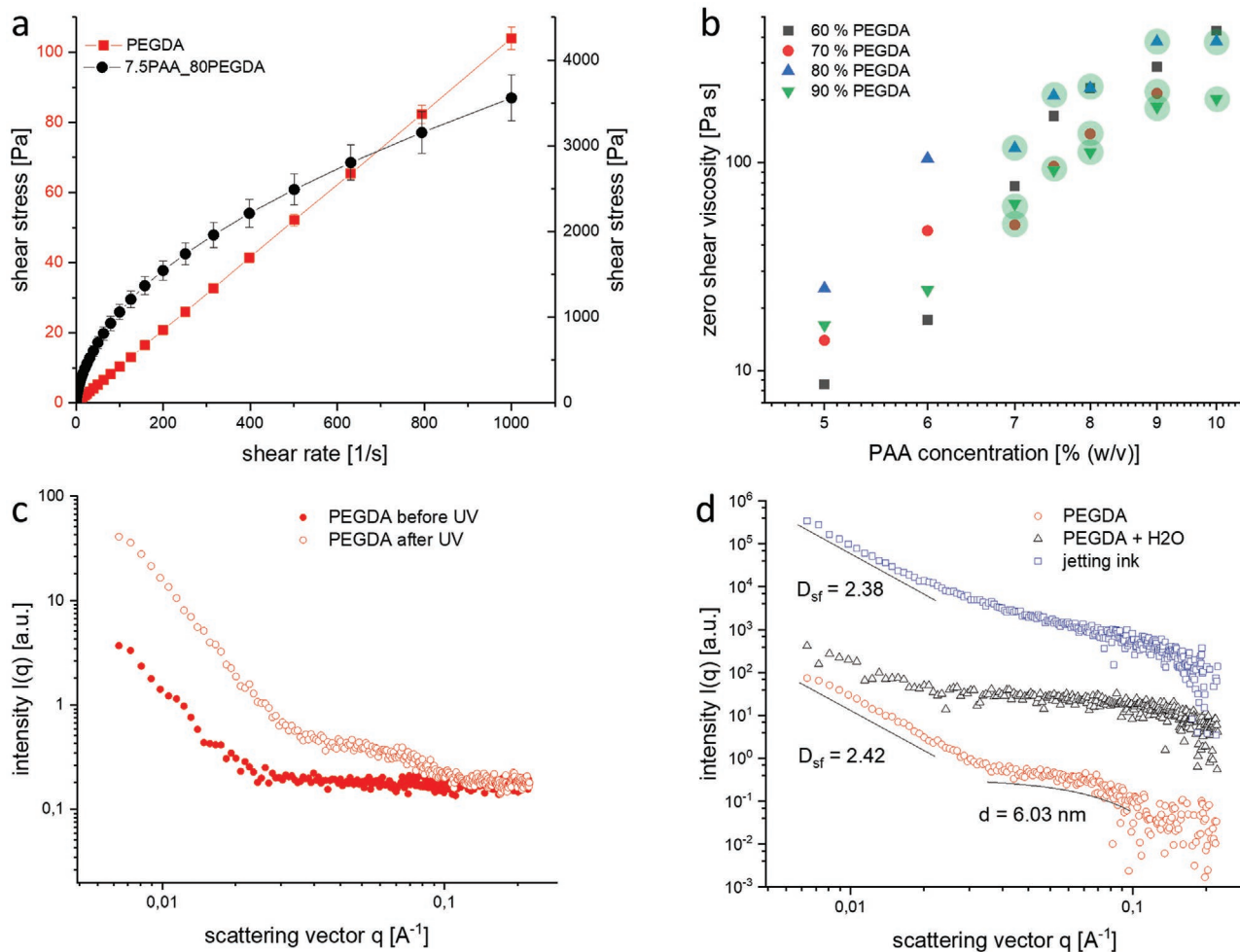
ADVANCED
SCIENCE NEWS
www.advancedsciencenews.com

Macromolecular
Bioscience
www.mbs-journal.de

Figure 2. a) Rheology measurements of pure PEGDA and PEGDA mixed with PAA. By adding PAA the Newtonian behavior of PEGDA get shifted to a shear thinning behavior and the viscosity increases to make it suitable for jetting. b) The zero shear viscosity data for variated PAA, PEGDA, and water ratios. The green marked samples are suitable for stable jetting while the jet of the other solutions beaks during the jetting process. c) Scattering data of PEG-DA before and after UV-curing. d) Scattering data and evaluation after background correction for PEG DA, PEG DA with water and the hydrogel ink.

poly(acrylic acid) (PAA) and is optimized and analyzed via rheological measurements for 3D jet writing. The hydrogel system is optimized by adjusting the architecture, water content capacity, and enzyme activity. Kinetic studies of entrapped enzymes in the scaffold show that proteins are still active after the high-voltage jetting process. Afterward, the mass transfer effects within the jetted hydrogels are estimated with resulting catalyst efficiencies and Thiele moduli. The enzymatic hydrogel scaffolds show minimal enzyme leakage and are active for a prolonged period of time in a bio flow reactor.

2. Electrohydrodynamic Jetting Solutions

The prerequisite for incorporating biologically active materials into structures is a water-based jet ink which maintains the stability and activity of the enzymes during the production process. Poly(ethylene glycol)diacrylate (PEGDA) was used as UV-crosslinkable macromere resulting in a hydrogel with high water absorption capacity owing to its uniform pore size.[29] The successful formation of the Taylor cone, and subsequently fibers, upon the application of the electric field, depends on the polymer concentration, nature of the solvent, conductivity and viscosity of the polymer solution.[30] On one hand, pure PEGDA (Mn = 700 g mol^{-1}) and PEGDA water combinations are not suitable for jetting due to low viscosity as shown in **Figure 2**. On the other hand, a mixture of PAA and PEGDA in water shows a sharp rise in viscosity and the solution shows shear thinning behavior that is necessary for hydrodynamic jetting.[31,32] The zero shear viscosity was determined to define a jetting window by varying the PAA, PEGDA, and water content of the jetting ink (Figure 2b). The green marked samples are suitable for stable jetting, while the jet of the other solutions was unstable. The results show a linear increase of the zero-shear viscosity by increasing the PAA concentration. PAA concentration of more than 7% [w/v] were necessary and a water content of 30% [v/v] or less was ideal for a stable jet process. Precisely, best experimental jetting results were achieved by using a PAA concentration of 7.5% [w/v] and a PEGDA to water content of 80:20% [v/v]
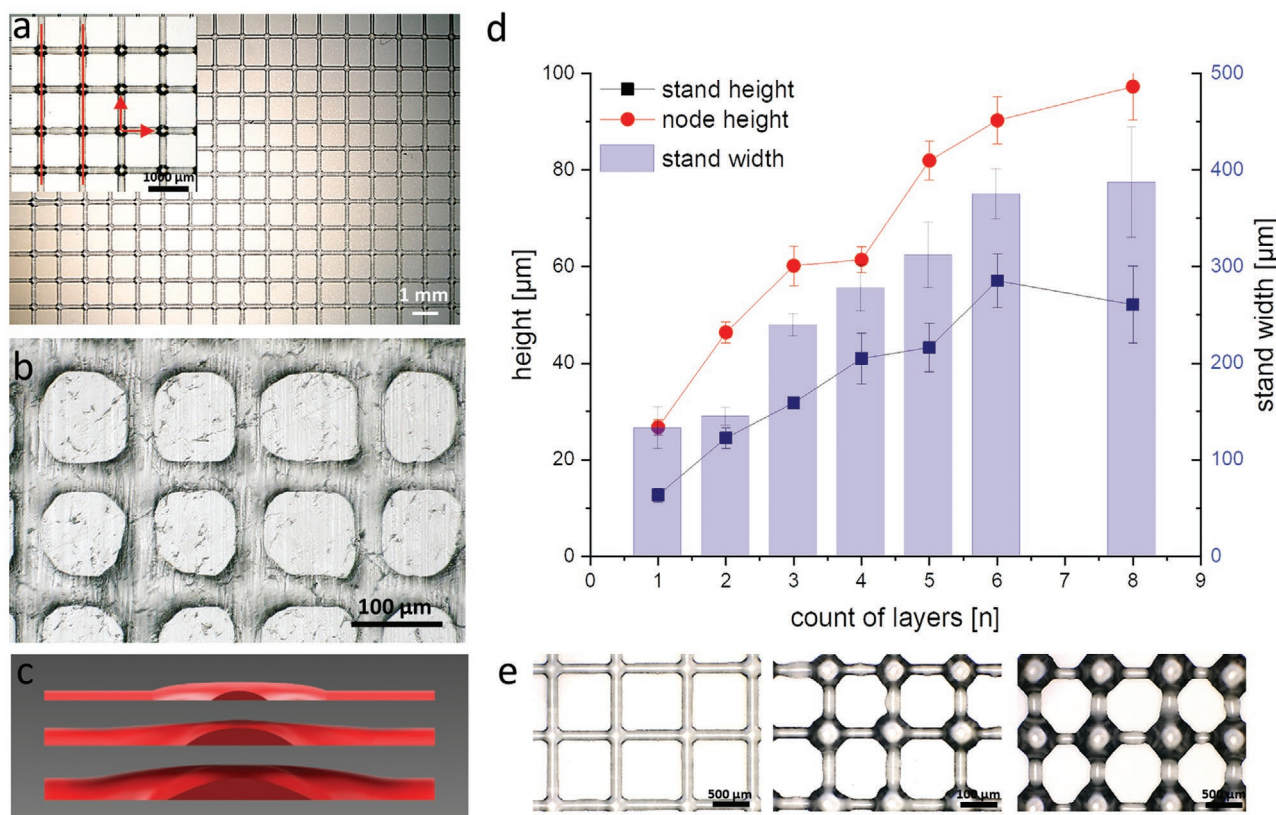
**ADVANCED
SCIENCE NEWS**
www.advancedsciencenews.com

**Macromolecular
Bioscience**
www.mbs-journal.de

Figure 3. Images of scaffold structures of hydrogel manufactured by 3D jet writing. a) High level of precision in fiber orientation and b) high-resolution placement. c) Schematic size comparison for scaffolds with cross sections of 2.2×10^3, 7.4×10^3, and 13.8×10^3 μm^2. d) Height specification of the strands and nodes as well as the strand width. e) Microscope images represented for one, three, and five-layer scaffolds.

which is used as jetting ink, unless otherwise specified, for the following experiments.

The suitability of an ink for an electrohydrodynamic jetting process depends on effective macromolecular entanglement. This leads to relatively high weight fractions of polymer compared to other hydrogel printing methods and can result in undesired aggregation of PEGDA. To evaluate the formation of PEGDA aggregated during radical polymerization, polymer solutions with and without PAA were studied by means of small-angle X-ray scattering (SAXS) measurements and were able to analyze the gel structure in a nondestructive manner in a size range between 1 and 130 nm. To characterize the influence of PEGDA on the internal structure change of the hydrogel ink induced during UV-curing, a selection of mixtures was analyzed, chosen to represent the specific components of the ink. The scattering data of PEGDA before and after UV-curing are given in Figure 2c. After UV-curing, PEGDA shows a significant scattering at larger scattering vectors ($q = 0.03–0.1$ A^{-1}) indicating a cluster size of ≈6 nm in diameter as well as a higher order of cluster size at lower scattering vectors ($q < 0.03$ A^{-1}). The evaluation of the scattering data after background correction for PEGDA, PEGDA with water, and the hydrogel ink is shown in Figure 2d. The cluster size of PEGDA and its shape is too large to be resolved. But the fractal dimension of the surface D_{sf} indicates a slightly roughened cluster surface ($D_{sf} = 2.42$). After the addition of water to the stock solution, both scattering

ranges disappeared. In the presence of PAA, scattering at lower scattering vectors ($q < 0.03$ A^{-1}) was detected. Comparable to the results obtained for the pure PEGDA solution, the cluster size and shape is too large to be resolved. But the fractal dimension of the surface D_{sf} indicates a smoother cluster surface ($D_{sf} = 2.38$) compared to pure PEGDA. Since PEGDA shows no scattering in the presence of water, it can be assumed that this scattering is due to the added PAA molecules. Thus, an influence of PEGDA in the hydrogel structure induced by PAA after UV-curing can be excluded.

3. Adjustable Micrometer-Scale Scaffold Architectures

The architecture of the dry scaffolds after crosslinking indicates a regular microstructure over a large jetting area as shown in **Figure 3**a. The individual strands have a linear orientation and cross at right angles (89.77 ± 0.13°) at the junctions with a 6.5 times thinner strand width compared to that of extrusion-based printing. The highest achievable jetting resolution is 120 µm measured from the centerline of two parallel strands (Figure 3b). UV-curing was performed under inert atmospheric conditions to solidify the scaffolds and ensuring absence of side reactions during the radical polymerization at the same time. In the presence of oxygen, it was not possible to harden the
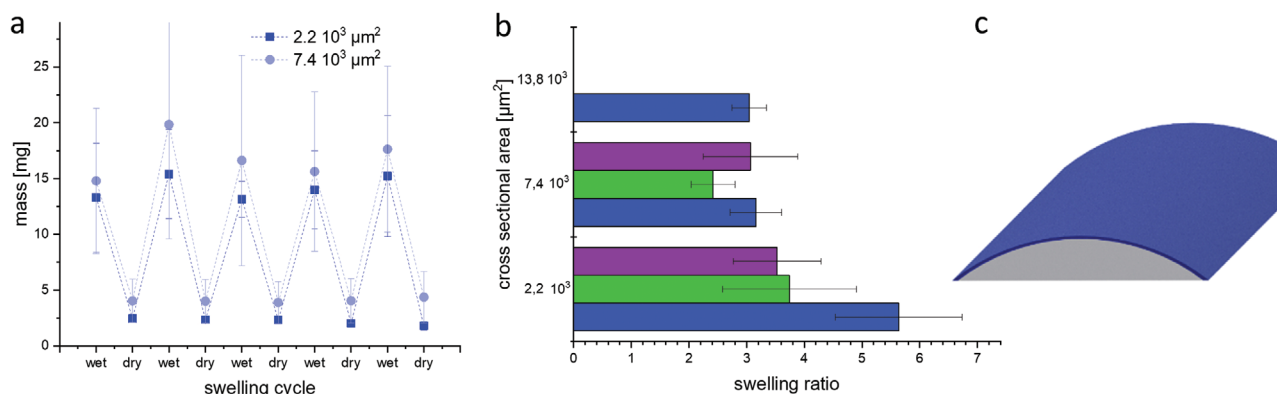
ADVANCED
SCIENCE NEWS
www.advancedsciencenews.com

Macromolecular
Bioscience
www.mbs-journal.de

Figure 4. Water adsorption capacity for hydrogel scaffold to create an attractive environment for biologically active materials. a) Mass data of dry and swollen scaffolds over several swelling cycle. b) Swelling ratio for different polymer ratios and fiber architectures. Ink composition: 7.5PAA_80PEGDA in blue, 10PAA_80PEGDA in green, and 10PAA_90PEGDA in purple. c) Schematic size comparison of a dry (gray) scaffold to the swollen scaffold (blue). The cross-sectional area of 2.2×10^3 μm^2 is increased by 15%.

micrometer-thin structures with this high surface-to-volume ratio. The scaffold was then detached, by cutting off the superfluous scaffold legs and peeling the scaffold off the collector glass slide while adding a drop of water resulting in stable free-standing 3D structures.

The height of the structure can be adjusted by the addition of more layers during the jetting process. Figure 3d shows the increasing height of the scaffold strands against the amount of jetted layers. A two-layer scaffold, for instance, results in a height of 24.5 ± 2.1 μm, a four-layer scaffold in 41.0 ± 5.3 μm, and six layers in 57.1 ± 5.6 μm. The height of the node points, i.e., the location where two of the strands cross, increased as well with increased stacking and was twice as high as the corresponding single strands. However, the width of the strands increased due to the high liquid content of PEGDA and water in the jetting ink. The ink may deliquesce slightly on the collector plate but it is still possible to stack up to ten layers in height due to the shear-thinning property of the ink. The cross section of the strand results in a circular segment with a cross-sectional area of 2.2×10^3 μm^2 for two layers, 7.4×10^3 μm^2 for four layers, and 13.8×10^3 μm^2 for six layers. The size comparison is schematically represented in Figure 3c and in accordance to the efficient shape of Lentikats.[33]

4. Enzymatic Batch Activity

In order to ensure the accessibility of small substrate molecules to the entrapped enzymes, and to guarantee the necessary aqueous environment, the water absorption capacity of the scaffolds is a critical factor. The wet and dry mass of scaffolds with cross-sectional areas of 2.2×10^3 and 7.4×10^3 μm^2 are shown in **Figure 4**a. The masses are reproducible over at least five cycles of swelling and drying. Independent of the architecture and the polymer composition, the scaffolds can uptake water around three times of their own dry weights (Figure 4b). Scaffolds with a cross-sectional area of 2.2×10^3 μm^2 and a low PAA concentration show a higher water uptake factor of 5.6 times.

By determining the architecture of a swollen single strand, a minimal anisotropic swelling is noticeable due to an increase in height of 9%, while the width increases only by 4%. The overall increase of the cross-sectional area thus amounts to $15\% \pm 3$ (Figure 4c). Thereby, we conclude that the developed hydrogel scaffold retains its stable 3D porous structure in the absence of water and additionally allows water to penetrate into the interstitial area due to its hydrophilic composition.

To determine the activity of entrapped active material, ß-galactosidase was used as a model enzyme. It was directly mixed into the jetting ink. The catalytic activity of the enzymatic scaffold was tested by the hydrolysis of the reactant o-nitrophenyl-β-D-galactopyranoside (oNPG) to ortho-nitrophenol (oNP) and galactose. The resulting yellow product oNP could then be detected by spectroscopy.

To demonstrate that the developed jetting ink is compatible with enzymes, ß-galactosidase was mixed into the jetting ink solution and the enzymatic activity of the solution was tested after stirring the ink for 1 h. The activity was then compared to the activity of the same amount of free enzyme, as well as jetted enzymes which had been redissolved. No activity loss due to ink toxicity or the applied high voltage of the electrohydrodymanic jetting was detected (**Figure 5**a).

The enzymatically active scaffolds show an increase of the product concentration over time, showing that enzymes are still active inside the support material (Figure 5b). Increased cross-sectional area of the scaffolds is directly correlated to product formation, which can be attributed to the increased single enzyme content per batch. However, the normalized enzyme activity increases with decreased cross-sectional area of the scaffold (Figure 5c). This is in parallel to the increase of the surface-to-volume ratio, and leads to the question if the reactant is accessible to all enzymes in the structure or only to the ones on the surface of the scaffold. To test this, scaffolds with different ink formulations, but the same size and architecture, were compared with each other in terms of their activity (Figure 5d). The results show an increase in the enzymatic activity with decreasing polymer concentration. Thus, the activity is influenced by the architecture and the material composition of the
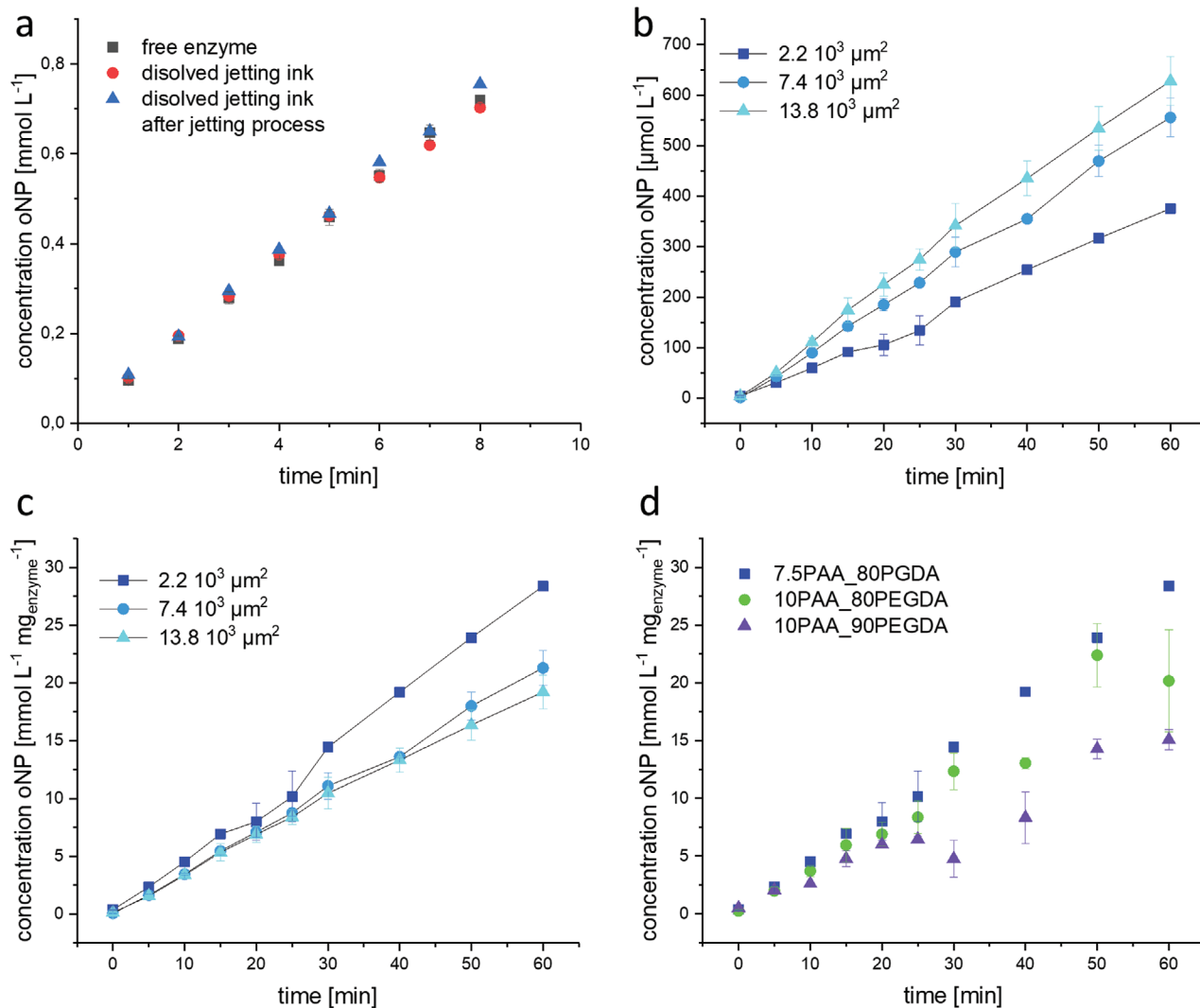
Figure 5. Activity measurements for entrapped ß-galactosidase inside the hydrogel scaffolds. a) Enzyme activity is fully retained under the conditions of 3D jet writing. b) oNP production of different scaffold architectures for direct comparison and normalized to the quantity of enzyme used in (c). d) oNP concentration data for different polymer ratios of the scaffold material.

scaffold. Neither the ink nor the jetting process had a negative effect on the enzyme activity.

5. Reactant Transport Capacity

An elementary cell of various scaffold architectures was digital replicated using computer-aided design and the diffusion of the reactants was subsequently simulated. The parameters were obtained by comparing the activity of enzyme-laden scaffolds to free enzymes in solution, which resulted in a catalytic efficiency of $21.2 \pm 4\%$ and a diffusion coefficient of 2.23×10^{-14} m^3 s^{-1} (see subsection Calculation and Simulation of Diffusion Properties in the Experimental section). The diffusion coefficient and the Thiele modulus of around 5 are lower compared to other PEGDA hydrogels, which is due to the high-molecular weight PAA content and the lack of swelling.[22,34,35]

The simulated diffusion of oNPG into a scaffold with a cross-sectional area of 2.2×10^3 μm^2 is shown in **Figure 6**a. The reactant oNPG diffuses into the scaffold over time and is converted into oNP by the enzymes, leading to a steady-state concentration after 1 h. The oNP molecule does not undergo any further enzymatic transformation, in contrast to the reactant, and can diffuse further inside the scaffold (Figure 6b+d). Here, the stationary state is achieved by concentration equilibrium to the surrounding medium. In doing so, product is lost in the scaffold, but this is experimentally negligible due to the relatively small volume of the scaffold compared to that of the surrounding medium.

Considering different strand architectures, the oNP concentration in the middle of the strand decreases by increasing the cross-sectional area (Figure 6c+e) due to the longer diffusion path required. It is noticeable that scaffolds with cross-sectional areas of 2.2×10^3 μm^2 have a significantly higher reactant
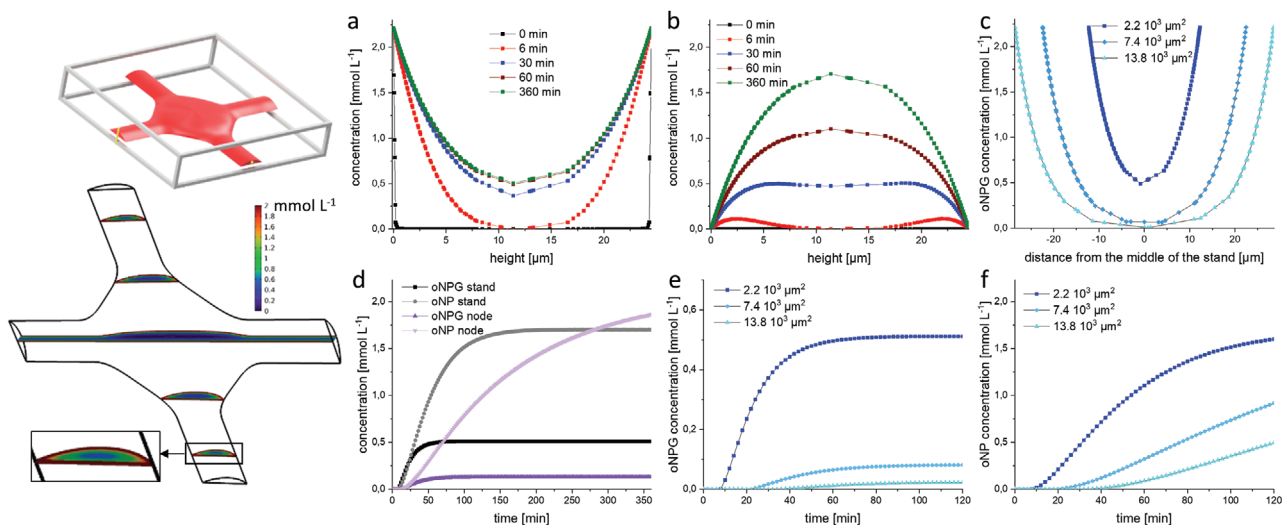
Figure 6. Simulating the diffusion of the reactant oNPG and product oNP visualizes the reactant and product distribution within the scaffold. a,b) Time-dependent oNPG and oNP concentration over the strand height represented for a scaffold with a cross-sectional area of 2.2×10^3 µm². c) Comparison of the oNPG concentration for different scaffold architectures after reaching steady state. Scaffold with a cross-sectional area of 2.2×10^3 µm² had the highest reactant concentration throughout. d) Time-dependent concentration patterns in the middle of the strand and node showing of scaffold with a cross-sectional area of 2.2×10^3 µm². e) The comparison of the temporal progression of the reactant for scaffolds with different architectures shows a direct correlation between higher oNPG concentrations, and smaller cross-sectional areas of the strand. The high accessibility of the reactants to enzymes results in high conversion rates and a rapid increase in the product concentration as shown in (f).

concentration in the interior of the strand than scaffolds with 7.4×10^3 and 13.8×10^3 µm² cross-sectional areas. This is likely due to the corresponding surface-to-volume ratios and fit the experimental activity record discussed before.

6. Long-Term Enzyme Stability

All previous calculations were based on the assumption that the enzyme is still completely retained in the hydrogel structure after exposure to an aqueous solution. In order to validate this assumption, the amount of protein in both the washing

and storage solution was determined (**Figure 7**a). The protein concentration in the washing and storage solution was found to be approximately the detection limit for all tested scaffolds. The only detectable protein loss was during detachment. Here, the bigger the cut cross sections, the higher the loss of enzymes. However, for the quantity of enzyme used, this loss appears to be negligible and no further enzyme is removed during additional washing steps and/or storage.

Bringing substrate accessibility, material properties, water adsorption capacity, stability, and architecture together, electrohydrodynamic jetted scaffolds with cross-sectional areas of 2.2×10^3 µm² consisting of 7.5% PAA and a PEGDA content
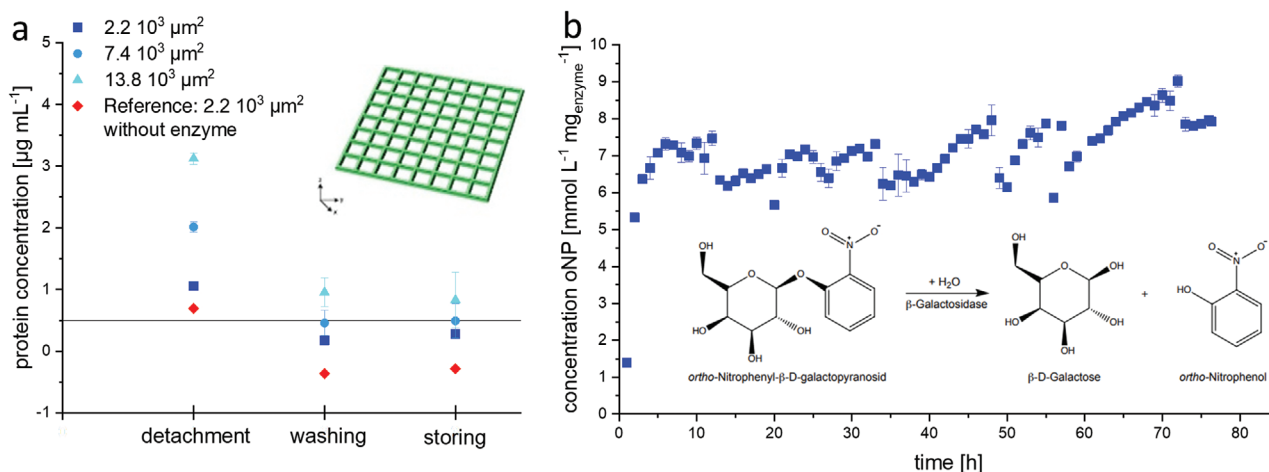

Figure 7. Long-term stability of immobilized enzymes inside an electrohydrodynamic jetted hydrogel scaffold. a) Leaching test by determining the enzyme concentration in the supernatant after washing and storing the scaffolds. No significant loss of enzyme can be detected after being detached from the glass slide. b) Product concentration data of a continuous flow reactor containing enzyme-loaded hydrogel scaffolds. A stable turnover as high as 50% over 76 h was achieved without any loss of enzyme activity or scaffold damage.

of 80% showed the highest activity. To test the long-term stability and activity of the entrapped enzymes, these scaffolds were placed inside a reactor with an applied continuous oNPG inflow. The converted product concentration in the outlet was recorded (Figure 7b). After 6 h, the oNP concentration was stable with around 7 mmol L^{-1} mg^{-1} enzyme, which corresponds to a turnover of 50%. This is around twice as high as comparable experiments with 3D-printed scaffolds.[36] The fluctuations of the recorded results are due to bleaching of the product solution during overnight hours. At the end of the experiments with a duration of 76 h, all scaffolds were still intact without any noticeable damage. We predict that the efficiency of the reactor can be further improved, by decreasing the flow rate or reactant concentration.

7. Conclusions

3D jet writing offers the possibility to create precise patterns of microsized polymer fibers using a water-based jetting ink. The fibers were orientated in freestanding scaffolds with reproducible architecture and adjustable pore sizes. Due to selected material properties, the scaffolds can absorb up to 5.6 times their own weight in water with minimal increase in their cross sectional diameters. Adding enzymes during the production step resulted in enzymatically active scaffolds with a catalytic efficiency of 21.2 ± 4%, without any overt leaching of enzymes. Further investigations showed that electrohydrodynamic jetted scaffolds with cross-sectional areas of 2.2×10^3 µm^2 consisting of 7.5% PAA and a PEGDA content of 80% showed the highest activity. The enzymatic scaffolds were demonstrated to be long-term active in a continuous reactor for 76 h with a stable turnover of 50%.

Further investigations should include widening the spectrum of biological substrates to examine the suitability of the hydrogel scaffolds for applications in diagnostics or enzymatic cascade reactions. Due to the used biocompatible materials and the good penetration of small molecules inside the scaffold strands, it should also be possible to entrap and culture living cells, as proof-of-concept experiments were able to prove.

8. Experimental Section

Materials: PAA (average M_v 450 000), PEGDA (average M_n 700), 2-hydroxy-4′-(2-hydroxyethoxy)-2-methylpropiophenone, β-galactosidase (EC 3.2.1.23) from *Aspergillus oryzae*, oNPG, and oNP were obtained from Sigma-Aldrich (Darmstadt, Germany). Ethanol, sodium citrate, NaOH, Na$_2$CO$_3$ (all analytical grade), and nitric acid (suprapure grade) were purchased from VWR (Radnor, Pennsylvania, USA). Deionized water was prepared with a Milli-Q Ultrapure system from Merck Millipore (Billerica, USA). All chemicals were used as received.

Ink Preparation: Different amounts of PAA were mixed with PEGDA until the solution was homogenously white. Then the ß-galactosidase water solution or pure water was added. To keep the enzyme activity comparable, an enzyme charge of 1.98 mg g^{-1} of dry matter yield of the hydrogel was used. Three different inks with different PAA and water to PEGDA ratios were investigated. The resulting volumes and masses are described in **Table 1**. Before using the ink, 80 µL of a freshly prepared 10% [w/v] 2-hydroxy-4′-(2-hydroxyethoxy)-2-methylpropiophenone in

Table 1. Composition of the different jetting inks with different PAA and water to PEGDA ratios. For nonenzymatic scaffolds, deionized water was used without ß-galactosidase.

	m_{PAA} [mg]	V_{PEGDA} [µL]	$V_{ß-Gal\ stock\ solution/water}$ [mL]	$c_{ß-Gal\ stock\ solution}$ [g L^{-1}]
7.5PAA_80PEGDA	120	1216	304	10
10PAA_80PEGDA	160	1216	304	10
10PAA_90PEGDA	160	1368	152	23

ethanol and water [70:30] solution was added as a radical initiator and left mixing for 10 min before jetting.

3D Jet Writing: A 3D jet writing setup as described in a previous work was used to produce the hydrogel scaffolds.[27] Briefly, a needle (ID = 0.84 mm, Nordson EFD, USA) was attached to a 1 mL syringe filled with the jetting ink and mounted on to a syringe pump (Harvard Apparatus, USA). The flowrate was set to 70 µL h^{-1} and the needle was charged to +7 kV using an external power source (FuG Elektronik, Germany). A grounded metal plate was mounted on a computer-assisted x–y stage (Newport Corporation, USA) with a distance of 8 cm to the needle. To control the bending and whipping instability during jet propagation, a secondary electric field was applied by placing a metal ring between the needle and collector. Charging the ring electrode to +3.5 kV created an electric potential well and reversed the direction of the electric field toward the center of the ring, suppressing the outward jet directed movement. Combining the stable polymer jet with a computer-assisted positioning system allowed precise patterning of the hydrogel fibers into highly ordered structures. For easier handling, a glass slide was placed on the collector and the scaffold was directly jetted onto it with a collector speed of 12 mm s^{-1}.

Extrusion-Based 3D Printing: To compare the width of 3D jet writing to a conventional extrusion-based printed hydrogel strand, the ink solution 7.5PAA_80PEGDA was printed with a pneumatic 3D printer (3D Discovery, regenHU, Villaz-St-Pierre, Switzerland). To achieve comparable results, the parameters were kept constant wherever possible. Therefore, extrusion was done through a needle with an inner diameter of 0.84 mm (Nordson EFD, USA), extrusion pressure of 0.04 MPa, initial height of 0.2 mm, and a printing speed of 12 mm s^{-1}. 50 mm long single strands were printed and the architecture was analyzed in the same way as the jetted scaffolds which resulted in a strand width of 858 ± 61 µm.

Crosslinking: To be able to cure the PEGDA of the thin scaffold strands, it was necessary to perform the radical chain reaction under inert conditions. For this, a custom-built reaction chamber was 3D-printed (Connex3 from Stratasys, Eden Prairie, MN). In this setup, nitrogen gas was diffused into a water bath and subsequently flowed over the scaffold sample in a closed environment. The sample was irradiated with a UV lamp (365 nm, 3 W, Fuyong Town, China) for 3 min. For enzyme activity tests, the samples were directly placed in water after crosslinking to avoid dehydration of the scaffolds.

Rheology: Flow curves of the hydrogel mixtures were obtained at 25 °C with a Physica MCR 301 plate rheometer with one plane plate and a CP-25-1 cone (Anton Paar GmbH, Graz, Austria) and a gap distance of 0.048 mm.

Rotational tests of pure PEGDA and the hydrogel ink (7.5PAA_80PEGDA) were sheared with a logarithmic shear rate gradient between 0.001 and 1000 s^{-1} which was applied over a duration of 5 min while measuring the shear stress.

The hydrogel ink with different PAA and water concentrations were initially sheared at a constant shear rate of 0.1 s^{-1} for 30 s followed by a resting period of 30 s to homogenize the starting conditions. Afterwards, a logarithmic shear rate gradient between 0.001 and 10 s^{-1} was applied over a duration of 267 s while measuring the resulting shear stress. The shear viscosity η was calculated by dividing the shear stress τ by the corresponding shear rate $\dot{\gamma}$. The zero shear viscosity η_0 is given by the limit value of the shear rate-dependent viscosity function at an infinitely low shear rate[37]

**ADVANCED
SCIENCE NEWS**

www.advancedsciencenews.com

**Macromolecular
Bioscience**

www.mbs-journal.de

$$\eta_0 = \lim_{\dot{\gamma} \to 0} \eta(\dot{\gamma}) \tag{1}$$

Small-Angle X-Ray Scattering: VSAXS measurements were performed in gel-holders with a Xeuss 2.0 (co. Xenocs, Grenoble, France). The sample-to-detector distance was set to 1000 mm. The scattering data were collected with a Pilatus 300 K detector (co. Dectris, Switzerland) for 600 s. The intensity $I(q)$ obtained by means of SAXS was measured as a function of the scattering vector q using the following equation

$$q = \frac{4\pi}{\lambda} * \sin\frac{\theta}{2} \tag{2}$$

where 2θ is the scattering angle and $\lambda = 0.154$ nm corresponds to the wavelength of the used Cu Kα X-ray beam. The data processing was done with Foxtrot software, while the analysis using IgorPro. The evaluation of the scattering data was based on the global unified fit model.[38–40] To fit the equation to several structural levels, each fit level i contains a Guinier regime to describe the structure size (e.g., primary particle or aggregates) and a power law regime to describe the inner (mass fractal) or outer structure features (surface fractal), given by

$$I(q) = \sum_{i=1}^{n}\left[G_i \cdot \exp\left(\frac{-q^2 R_{gi}^2}{3}\right) + B_i \cdot \exp\left(\frac{-q^2 R_{g(i+1)}^2}{3}\right) \cdot \left\{\frac{q}{\left[\mathrm{erf}\left(q R_{gi}/\sqrt{6}\right)\right]^3}\right\}^{-p_i}\right] \tag{3}$$

with the radius of gyration R_{gi}, the error function erf, the Guinier prefactor G_i, and the prefactor specific to the power-law scattering B_i with an exponent p_i. The particle size is given by

$$d_p = 2\sqrt{\frac{5}{3}} R_g \tag{4}$$

In case of particles or clusters, in lower q-ranges the exponent p describes the form factor $P(q)$. For spheres, the form factor is given by 0, 1 describes a cylindrical, and 2 a disc-like shape.[41] The fractal properties of a single cluster can be described by the fractal dimension of the surface D_{sf} and is given by[42]

$$D_{sf} = 6 - p \tag{5}$$

Characterization of the Scaffold Architecture: Overview images were taken with an upright optical microscope Keyence VHX 5000 (Neu-Isenburg, Germany). The angles at the junctions of the scaffolds were measured using ImageJ (open-source software).

For cross-sectional analysis, the dry scaffolds were cut with a fresh razor blade and observed with the optical microscope in a wet and dry state. With the Keyence software (version 1.8.0) the strand width s, the strand height h, the radius R, and the arc length b were measured. The cross-sectional area of the strands was calculated with the given formula for circular segments A

$$A = R^2 * \arcsin\left(\frac{s}{2R}\right) - \frac{s * (R - h)}{2} \tag{6}$$

Scanning Electron Microscopy: The hydrogel scaffolds were attached to a sample holder using carbon-containing adhesive pads. They were coated with 4 to 5 nm gold-palladium [80:20] carried out at 21.3 mA for 32 s using a MED 020 device (Bal-Tec AG, Balzers, Liechtenstein) to improve the conductivity. The images were taken with a VEGA 3 from TESCAN (Dortmund, Germany) with a beam intensity of 10, a voltage of 8.0 kV, and a working distance of 7 mm.

Swelling Properties: To determine the swelling factor, the hydrogel scaffolds were placed in water at room temperature for 15 h. Excess water was removed with a tissue and the wet mass m_w was measured with a Pioneer (Ohaus, USA). The scaffolds were then dried in a drying cabinet (T12 Kendro, Heraeus instruments) at 40 °C for 7 h and weighed again to determine the dry mass m_d. This was repeated over five cycles for each sample. The swelling factor Q was calculated using the following equation

$$Q = \frac{m_w - m_d}{m_d} \tag{7}$$

Leaching Tests Using Micro BCA: A drop of water (0.65 mL) was put on each produced scaffold to peel it off the glass slide. After 5 min, the scaffold was transferred to a new water bath (1 mL) and incubated for 15 min. Then the scaffold was stored overnight in a new water bath (1 mL) in the fridge at 8 °C before using it for enzyme kinetics or for the continuous reactor. To determine the amount of washed out enzyme, a micro BCA assay (Micro BCA Protein Assay Kit, Pierce Biotechnology, Rockford, IL) of each washing solution was performed.

Enzyme Kinetics of Free and Immobilized Enzymes: For determination of batch kinetics, plain enzyme solutions as well as jetted hydrogel structures with entrapped enzyme were tested for their enzymatic activity. In addition to the enzymatic activity of the scaffolds, the loss of enzyme activity during the jetting process was also determined. Therefore, scaffolds were produced and the activity was tested before crosslinking by dissolving them. This was compared to the same amount of hydrogel ink before jetting and to the activity of free enzyme. The tests were done in 1.8 mL of citrate buffer (333 × 10^{-3} M sodium citrate titrated against NaOH to pH 4.6) containing the reactant oNPG at a concentration of 2.2 mmol L^{-1}. The enzyme catalyzes the reaction of oNPG hydrolysis to oNP and galactose. The experiments were done at 37 °C in an Eppendorf thermoshaker (Eppendorf, Hamburg, Germany) at 750 rpm. Samples of 25 or 50 μL were taken over a period of 1 h. These aliquots were added to 100 μL of 1 M sodium carbonate solution in microtiter plates and filled up with citrate buffer to a final volume of 200 μL. UV–vis spectra of the solutions were measured at 420 nm to monitor the absorption profile and intensity of the oNP product.[22] Using a commercially available oNP, a calibration curve was determined to consequently quantify the concentration. As the effective extinction coefficient may change in presence of solutes and dispersed particles, hydrogel scaffolds without enzymes were tested as a reference.

Continuous Reactor: A flow reactor with a reaction volume of 3 mL was used to investigate the long-term activity of the entrapped enzymes. The reactor was 3D-printed with VeroWhitePlus RGD835 (Stratasys, Eden Prairie, MN) as described in other publications.[36,43] Due to adsorption effects,[36] the reactor was rinsed with oNP solution for several hours to guarantee a completely saturated reactor wall. Before the start of the experiment, the reactor was rinsed with citrate buffer until no oNP was no longer detectable in the outlet. 14 hydrogel scaffolds (cross-sectional area: 2.2 × 10^3 μm^2) were placed in the reaction chamber. The reactor as well as the inlet and outlet tubes were filled with citrate buffer and rinsed to get rid of air bubbles. The whole system was heated to 37 °C in a water bath (E100, Lauda Dr. R. Wobser GmbH & Co. KG, Germany). A syringe containing the dissolved reactant in citrate buffer was connected to the inlet and a flow rate of 3 mL h^{-1} which corresponds to a oNPG mass flow of 6.64 × 10^{-3} mmol h^{-1} was applied. The oNP containing outflow was fractioned in 3 mL samples with an automatic fraction collector (Superfrac, Pharmacia Biotech AB, Sweden) and the oNP concentration was measured as mentioned before. Due to bleaching effects of oNP, the samples were analyzed immediately throughout the day. The collected samples during night hours were measured in the morning. The total duration of the experiments was 76 h, with the substrate solution being remade twice a day.

Calculation and Simulation of Diffusion Properties: For the simulation of the diffusion behavior, the elementary cell of the hydrogel scaffolds was designed in the 3D CAD software Inventor 2019 Professional (Autodesk Inc., San Rafael, CA) based on the data from the image analysis. The software generates 3D shapes which are saved in the *.ipt data format that can be directly imported into the simulation software COMSOL Multiphysics 5.4 (COMSOL AB, Stockholm, Sweden). Global Parameters were defined as stated. The surface area and the volume of the designed hydrogel nodes were calculated in the iParameters included in Inventor with the setting "high accuracy." The diffusion coefficient was calculated from batch kinetic experiments. The initial reaction rate of the hydrogel lattices was compared to the reaction rate of enzyme in solution, which resulted in an effectiveness factor of around 21.2%. As a rough estimate,

the diffusion distance from the surface of the hydrogel to the center of one strand was about 15 µm for the structures with a cross-sectional area of 2.2×10^3 µm^2. Reaction constant k [s^{-1}] for the enzymatic reaction, characteristic length of diffusion L [m], and diffusion coefficient [m^2 s^{-1}] form the dimensionless number Thiele modulus ϕ, which can also be mathematically derived from the effectiveness factor η_{cat}. It correlates the enzymatic activity of immobilized enzymes to the activity of free enzymes in solution. For diffusion-limited systems of Thiele moduli > 3, first-order reaction kinetics and a catalyst slab η_{cat} can be simplified by the following equation[44]

$$\eta_{cat} = \frac{\tan h(\phi)}{\phi} \tag{8}$$

$$D_{eff} = k * \left(\frac{L}{\phi}\right) \tag{9}$$

Solving the set of equations yielded the effective diffusion coefficient of 2.23×10^{-14} m^3 s^{-1}. These global parameters were included in COMSOL into the equations of the "transport of diluted species in porous media" physics to describe the time-dependent transport and reaction processes within the hydrogel geometry. As boundary conditions initial concentrations were set to c_reactant = 2.2 mmol L^{-1} on the surface and no reactant or product within the structure. Diffusion was chosen as regime for mass transport and Michaelis-Menten kinetics of first order for the enzymatic reaction ($k = 7.33 \times 10^{-4}$ s^{-1}). The mesh of the geometry consisted of the automatic setting "fine mesh" (maximal element size of 2×10^{-5}, element growth rate of 1.4, curvature factor of 0.4, scaling 1 for all dimensions) and 12 surface layers (thickness value of 0.2×10^{-6} m (scaffolds with cross-sectional area of 2.2×10^3 µm^2) and 0.4×10^{-6} m (all others)). The product profile was evaluated through the middle of the node and through the middle of the strand.

Conflict of Interest

The authors declare no conflict of interest.

[1] R. Ravindran, A. K. Jaiswal, *Enzym. Fuel Cells*, Materials Research Forum, Millersville, PA, USA **2019**, pp. 51–72.

[2] M. Bilal, M. Asgher, R. Parra-Saldivar, H. Hu, W. Wang, X. Zhang, H. M. N. Iqbal, *Sci. Total Environ.* **2017**, *576*, 646.

[3] R. A. Sheldon, *Adv. Synth. Catal.* **2007**, *349*, 1289.

[4] M. Peng, E. Mittmann, L. Wenger, J. Hubbuch, M. K. M. Engqvist, C. M. Niemeyer, K. S. Rabe, *Chem. Eur. J.* **2019**, *25*, 15998.

[5] K. S. Rabe, J. Müller, M. Skoupi, C. M. Niemeyer, *Angew. Chem., Int. Ed.* **2017**, *56*, 13574.

[6] N. J. Burgoyne, R. M. Jackson, *From Protein Structure to Function with Bioinformatics*, Springer, Netherlands **2009**, pp. 167–186.

[7] R. A. Sheldon, S. van Pelt, *Chem. Soc. Rev.* **2013**, *42*, 6223.

[8] R. A. Sheldon, J. M. Woodley, *Chem. Rev.* **2018**, *118*, 801.

[9] D. Weiser, F. Nagy, G. Bánóczi, M. Oláh, A. Farkas, A. Szilágyi, K. László, Á. Gellért, G. Marosi, S. Kemény, L. Poppe, *Green Chem.* **2017**, *19*, 3927.

[10] P. Tufvesson, J. Lima-Ramos, M. Nordblad, J. M. Woodley, *Org. Process Res. Dev.* **2011**, *15*, 266.

[11] P. K. Robinson, *Essays Biochem.* **2015**, *59*, 1.

[12] K. F. O'Driscoll, *Methods Enzymol.* **1976**, *44*, 169.

[13] N. R. Mohamad, N. H. C. Marzuki, N. A. Buang, F. Huyop, R. A. Wahab, *Biotechnol. Biotechnol. Equip.* **2015**, *29*, 205.

[14] A. C. Pierre, G. M. Pajonk, *Chem. Rev.* **2002**, *102*, 4243.

[15] N. Ganonyan, N. Benmelech, G. Bar, R. Gvishi, D. Avnir, *Mater. Today* **2020**, *33*, 24.

[16] F. Ishizuka, R. Chapman, R. P. Kuchel, M. Coureault, P. B. Zetterlund, M. H. Stenzel, *Macromolecules* **2018**, *51*, 438.

[17] M. J. Sawkins, L. T. Saldin, S. F. Badylak, L. J. White, in *Extracell. Matrix Tissue Eng. Biomater.*, Humana Press, Cham, **2018**, pp. 27–58.

[18] I. Bhushan, R. Parshad, G. N. Qazi, V. K. Gupta, *J. Bioact. Compat. Polym.* **2008**, *23*, 552.

[19] M. Schlieker, K.-D. Vorlop, in *Immobil. Enzym. Cells*, Humana Press, Totowa, New Jersey **2006**, pp. 333–343.

[20] H. Gröger, E. Capan, A. Barthuber, K. D. Vorlop, *Org. Lett.* **2001**, *3*, 1969.

[21] A. Urrios, C. Parra-Cabrera, N. Bhattacharjee, A. M. Gonzalez-Suarez, L. G. Rigat-Brugarolas, U. Nallapatti, J. Samitier, C. A. Deforest, F. Posas, J. L. Garcia-Cordero, A. Folch, *Lab Chip* **2016**, *16*, 2287.

[22] B. Schmieg, A. Schimek, M. Franzreb, *Eng. Life Sci.* **2018**, *18*, 659.

[23] S. N. Jayasinghe, *Analyst* **2013**, *138*, 2215.

[24] A. Townsend-Nicholson, S. N. Jayasinghe, *Biomacromolecules* **2006**, *7*, 3364.

[25] M. M. Hohman, M. Shin, G. Rutledge, M. P. Brenner, *Phys. Fluids* **2001**, *13*, 2201.

[26] A. Steier, A. Muñiz, D. Neale, J. Lahann, *Adv. Mater.* **2019**, *31*, 1806898.

[27] J. H. Jordahl, L. Solorio, H. Sun, S. Ramcharan, C. B. Teeple, H. R. Haley, K. J. Lee, T. W. Eyster, G. D. Luker, P. H. Krebsbach, J. Lahann, *Adv. Mater.* **2018**, *30*, 1707196.

[28] J. Lee, S. Y. Lee, J. Jang, Y. H. Jeong, D. W. Cho, *Langmuir* **2012**, *28*, 7267.

[29] S. J. Rukmani, P. Lin, J. S. Andrew, C. M. Colina, *J. Phys. Chem. B* **2019**, *123*, 4129.

[30] A. Haider, S. Haider, I. K. Kang, *Arabian J. Chem.* **2018**, *11*, 1165.

[31] G. I. Taylor, *Proc. R. Soc. London, Ser. A* **1964**, *280*, 383.

[32] J. M. Deitzel, J. Kleinmeyer, D. Harris, N. C. B. Tan, *Polymer* **2001**, *42*, 261.

[33] V. Krasňan, R. Stloukal, M. Rosenberg, M. Rebroš, *Appl. Microbiol. Biotechnol.* **2016**, *100*, 2535.

[34] G. M. Cruise, D. S. Scharp, J. A. Hubbell, *Biomaterials* **1998**, *19*, 1287.

[35] S. M. Evans, A. L. Litzenberger, A. E. Ellenberger, J. E. Maneval, E. L. Jablonski, B. M. Vogel, *Mater. Sci. Eng., C* **2014**, *35*, 322.

[36] B. Schmieg, J. Döbber, F. Kirschhöfer, M. Pohl, M. Franzreb, *Front. Bioeng. Biotechnol.* **2019**, *6*, 211.

[37] T. G. Mezger, *The Rheology Handbook, 4th ed.*, Vincentz Network, Hanover, Germany **2014**.

[38] G. Beaucage, D. W. Schaefer, *J. Non-Cryst. Solids* **1994**, *172*, 797.

[39] G. Beaucage, *J. Appl. Crystallogr.* **1995**, *28*, 717.

[40] G. Beaucage, *J. Appl. Crystallogr.* **1996**, *29*, 134.

[41] B. Hammouda, *J. Appl. Crystallogr.* **2010**, *43*, 716.

[42] P. W. Schmidt, *J. Appl. Crystallogr.* **1991**, *24*, 414.

[43] F. Kazenwadel, E. Biegert, J. Wohlgemuth, H. Wagner, M. Franzreb, *Eng. Life Sci.* **2016**, *16*, 560.

[44] D. Murzin, T. Salmi, *Catalytic Kinetics*, Elsevier Science, Amsterdam, Netherlands **2005**, pp. 341–418.